





ARTICLE

DOI: 10.1038/s41467-018-07075-3

OPEN

Photoreduction of gaseous oxidized mercury changes global atmospheric mercury speciation, transport and deposition

Alfonso Saiz-Lopez ¹, Sebastian P. Sitkiewicz^{2,3}, Daniel Roca-Sanjuán³, Josep M. Oliva-Enrich¹, Juan Z. Dávalos¹, Rafael Notario¹, Martin Jiskra ⁴, Yang Xu⁴, Feiyue Wang ⁵, Colin P. Thackray ⁶, Elsie M. Sunderland⁶, Daniel J. Jacob⁶, Oleg Travnikov⁷, Carlos A. Cuevas¹, A. Ulises Acuña¹, Daniel Rivero¹, John M.C. Plane⁸, Douglas E. Kinnison⁹ & Jeroen E. Sonke⁴

Anthropogenic mercury (Hg(0)) emissions oxidize to gaseous Hg(II) compounds, before deposition to Earth surface ecosystems. Atmospheric reduction of Hg(II) competes with deposition, thereby modifying the magnitude and pattern of Hg deposition. Global Hg models have postulated that Hg(II) reduction in the atmosphere occurs through aqueous-phase photoreduction that may take place in clouds. Here we report that experimental rainfall Hg(II) photoreduction rates are much slower than modelled rates. We compute absorption cross sections of Hg(II) compounds and show that fast gas-phase Hg(II) photolysis can dominate atmospheric mercury reduction and lead to a substantial increase in the modelled, global atmospheric Hg lifetime by a factor two. Models with Hg(II) photolysis show enhanced Hg(0) deposition to land, which may prolong recovery of aquatic ecosystems long after Hg emissions are lowered, due to the longer residence time of Hg in soils compared with the ocean. Fast Hg(II) photolysis substantially changes atmospheric Hg dynamics and requires further assessment at regional and local scales.

¹Department of Atmospheric Chemistry and Climate, Institute of Physical Chemistry Rocasolano, CSIC, Madrid 28006, Spain. ²Kimika Fakultatea, Euskal Herriko Unibertsitatea UPV/EHU and Donostia International Physics Center (DIPC), P.K. 1072, Euskadi, 20080 Donostia, Spain. ³Institut de Ciència Molecular, Universitat de València, Valencia 46071, Spain. ⁴Géosciences Environnement Toulouse, CNRS/OMP/Université de Toulouse, 31400 Toulouse, France. ⁵Department of Environment and Geography, Centre for Earth Observation Science, University of Manitoba, Winnipeg, MB R3T 2N2, Canada. ⁶Harvard John A. Paulson School of Engineering and Applied Sciences, Harvard University, Cambridge, MA 02138, USA. ⁷Meteorological Synthesizing Centre - East of EMEP, Moscow 115419, Russia. ⁸School of Chemistry, University of Leeds, Leeds LS2 9JT, UK. ⁹Atmospheric Chemistry Observations and Modelling, NCAR, Boulder, CO 80301, USA. Correspondence and requests for materials should be addressed to A.S.-L. (email: a.saiz@csic.es)

Atmospheric mercury, a contaminant of global concern, is primarily emitted in the gaseous elemental Hg(0) form, with smaller contributions of gaseous oxidized Hg(II) and particle-bound Hg(II)^{1,2}. Gaseous oxidized Hg(II)XY compounds may contain a variety of X,Y halogen atoms or oxygen-containing species, including Br, BrO, Cl, I, O, OH, HO₂, NO₂, and organic groups. Due to the low ambient concentration (pg m⁻³), gaseous oxidized Hg(II) compounds have only been identified as HgCl₂ and HgBr₂ in urban and indoor air³ and as HgCl₂ in power plant plumes⁴. The atmospheric Hg(0) and Hg(II) forms have markedly different water solubility, chemical reactivity and lifetime against deposition. The lifetime of Hg(0) against deposition is in the range of several months to over a year, whereas that of Hg(II) compounds is on the order of days to weeks⁵. Eventually, Hg(0) is oxidized to Hg(II) compounds, which are soluble, partition into aerosol, and deposit readily both by dry and wet mechanisms. Direct assimilation of Hg(0) by plants and oceans is also thought to be important^{6,7}. The long lifetime of Hg(0) leads to Hg deposition far from its emission sources to remote ecosystems, including the open oceans and polar regions. In aquatic ecosystems, Hg(II) is methylated and may be biomagnified up the food chain to levels that induce toxic effects in wildlife and humans⁸.

The development of atmospheric chemistry and transport models (CTMs), an important tool for understanding global Hg cycling and predicting future Hg exposure, has drawn much attention to the mechanistic aspects of Hg(0) oxidation. While gas-phase O₃, OH, HO₂, H₂O₂, and NO₃ are all potential Hg(0) oxidants^{6,9–11}, the oxidation process under atmospheric conditions is thought to be initiated primarily via photolytically produced atomic bromine by a two-stage mechanism (Fig. 1)^{6,11–13}. In the first step, the dominant reaction to produce gaseous oxidized Hg(II) compounds is thought to be the oxidation of Hg(0) by bromine atoms, yielding the unstable intermediate HgBr. This radical can be readily dissociated back to Hg(0), but HgBr can also be competitively oxidized by other major radical oxidant species in the atmosphere (e.g. OH, Br, I, Cl, NO₂, HO₂, BrO, IO, and ClO) to a series of currently-assumed stable Hg(II) compounds, as shown in Fig. 1:

Much less is known about the reduction of Hg(II) compounds to Hg(0) in the atmosphere. Global Hg CTMs, based on Hg(0) oxidation alone, predict an unrealistically short residence time of Hg(0), and the simulated spatiotemporal Hg(0) variations would not match observations⁶. To reconcile such differences, these models need to include an adjustable term to account for Hg(II) reduction in the atmosphere. Such reduction has been presumed to occur in the aqueous phase of clouds^{6,10,14}. Faster gas-phase Hg(0) oxidation kinetics has led to the need of these models to employ ever faster in-cloud Hg(II) reduction⁶, with maximum rate constants > ~1–3 h⁻¹, corresponding to in-cloud Hg(II) lifetimes <1 h on a global mean basis (see SI). Although aqueous Hg(II) photoreduction in Earth's surface waters is a well-documented process¹⁵, little experimental or observational evidence exists in the case of atmospheric liquid water¹⁶. Earlier

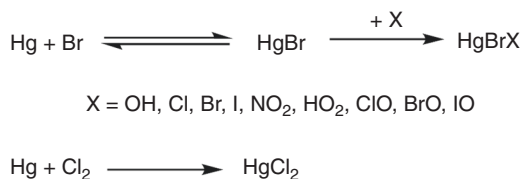


Fig. 1 Current understanding of the formation of oxidized Hg(II) compounds from atmospheric gaseous elemental mercury initiated by different oxidant species. This figure also includes other secondary oxidation mechanisms involving single-step reactions with Cl₂, O₃, BrO, and ClO

studies suggested that Hg(II) reduction could proceed via aqueous SO₃ and HO₂ reaction pathways^{16,17}, but these pathways are now considered irrelevant at the global scale⁶. Therefore, the significance of atmospheric aqueous Hg(II) reduction and the validity of their inclusion in the global mercury CTMs has been questioned^{6,17,18}.

None of the global mercury models has been used to test the possibility of an alternative explicit gas-phase photoreduction of Hg(II) compounds, due to the poor understanding of its mechanism and reaction rates⁶. The most recent studies—albeit 27 years ago—suggested the absence of gas-phase photoreduction for HgCl₂ and Hg(CN)₂ and slow photoreduction rates^{19,20} for Hg(OH)₂ and Hg(SH)₂, despite an earlier study of the UV absorption cross sections which suggested that HgBr₂ and HgI₂ could undergo relatively fast photolysis^{21,22}. As far as we are aware there have been no further experimental or theoretical studies on the photolytic properties of Hg(II) compounds of atmospheric relevance.

Here, we revisit the photoreduction pathways of atmospheric Hg(II) compounds. First, we show that irradiation experiments with boundary layer and free tropospheric rainwater do not support fast aqueous-phase Hg(II) photoreduction. We then compute the UV-VIS absorption cross sections of the following Hg(II) compounds: HgCl₂, HgBr₂, HgBrOCl, HgBrI, HgBrOBr, HgBrOI, HgBrNO₂, HgBrONO, HgBrOH, HgBrOOH, and HgO, using high-level quantum chemical methods, and infer the corresponding atmospheric photoreduction rates. Our results show for the first time that gas-phase Hg(II) photoreduction can proceed at relevant timescales, and is more important than in-cloud Hg(II) photoreduction. The inclusion of this new gaseous-phase Hg(II) photoreduction mechanism in two state-of-the-art global Hg models reveals major implications for our understanding of Hg cycling in the atmosphere, and its deposition to the surface environment.

Results

Laboratory rainfall Hg(II) photoreduction experiments. To study aqueous phase Hg(II) photoreduction, ten rainfall events were sampled in suburban Toulouse and at the high altitude (2877 m) Pic du Midi Observatory (PDM, France) in the summer of 2017. Rainfall samples were irradiated in a quartz reactor with natural sunlight or with a solar simulator (see Methods). We observe (Supplementary Figure 1a and 1b, Supplementary Data 1 and Supplementary Table 1) no statistically significant differences between rainfall Hg(II) reduction rates under natural (0.063 ± 0.013 h⁻¹) and simulated sunlight (0.037 ± 0.016 h⁻¹), and for filtered (0.058 ± 0.011 h⁻¹) and unfiltered (0.039 ± 0.020 h⁻¹) suburban rainwater (*t*-test, all *p* > 0.05). The mean photochemical reduction rate of suburban rainfall was 0.051 ± 0.019 h⁻¹ (σ, *n* = 10). The mean rate at the remote PDM samples was two-fold higher, 0.15 ± 0.01 h⁻¹ (σ, *n* = 3), than that of the suburban Toulouse samples, and three times slower than the median photoreduction rate of 0.41 h⁻¹ (*n* = 24) for inland and marine waters¹⁵. Our experimental rainwater photoreduction rates, under fully sunlit conditions, are an order of magnitude slower than the optimized maximum in-cloud photoreduction rate^{6,23} of > 1.0 h⁻¹ in global Hg CTMs.

Quantum chemical computation of gaseous Hg(II) absorption cross sections. We now turn to the computation of electronic spectra and absorption cross sections of gas-phase Hg(II) compounds which are required to estimate the corresponding photoreduction rates. A summary of the UV-VIS spectra and absorption cross sections, computed at the CASSCF/MS-CASPT2/SO-RASSI level of theory (Methods), is presented

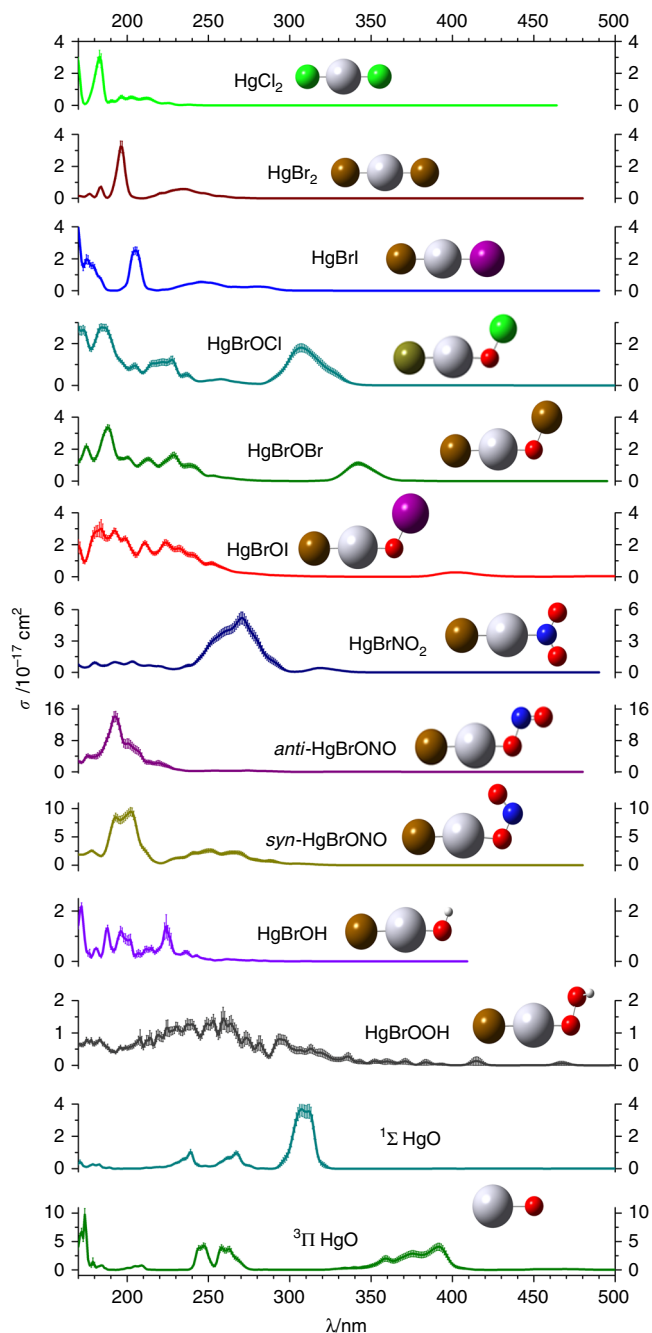


Fig. 2 Ball-and-stick representation and computed UV-VIS absorption spectra and cross sections (σ , cm^2) of the Hg(II) compounds studied in the present work. The light-coloured areas correspond to the uncertainty of the cross section due to the statistical sampling. Note the different range of σ values for some of the spectra. Also note that only wavelengths >290 nm are relevant for ambient tropospheric conditions

in Fig. 2 for the 170–600 nm wavelength range. The calculated spectra of HgCl_2 and HgBr_2 are in very good agreement with previous experimental^{22,24–26} and computed spectra²¹ (Fig. 3), thus providing strong support for the theoretical method applied here. The majority of the spectra consist of well-defined absorption bands in the 200–350 nm range, which are red-shifted when Cl is replaced with Br and I atoms. Note that three different isomers could form from the reaction of HgBr with NO_2 : HgBrNO_2 , and *syn*- and *anti*- HgBrONO . However, high-

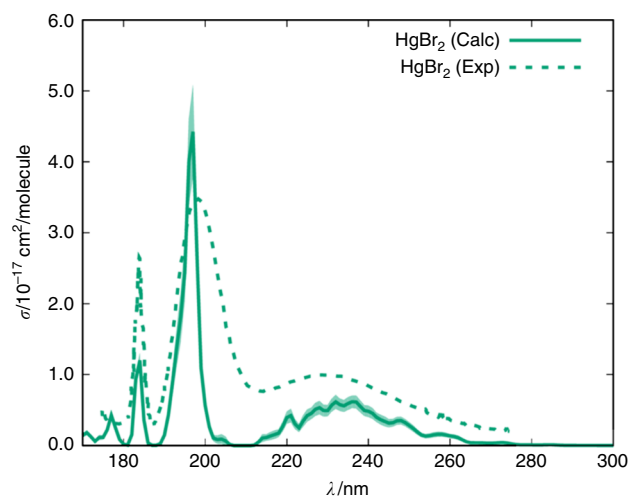


Fig. 3 Calculated and experimental cross section of gas-phase HgBr_2 . The calculated spectrum was obtained with the CASSCF/MS-CASPT2/SO RASSI methodological approach using the ANO-RCC-VTZP basis set. The light coloured areas correspond to the numerical error of absorption cross sections due to the statistical sampling

level quantum chemical computations²⁷ indicate that *syn*- HgBrONO is the most thermodynamically stable species.

Computation of photolysis rates and atmospheric lifetime of Hg(II) compounds. The annually averaged atmospheric lifetimes against photolysis in the troposphere for the Hg(II) compounds studied here are presented in Fig. 4 (see also Supplementary Table 2 and Supplementary Figure 2 for zonal-averaged atmospheric lifetimes). The species with the longest lifetime is HgCl_2 (48 years), and the species with the shortest lifetime is HgBrOBr (<1 s). These lifetimes were calculated assuming a complete UV-VIS photodissociation under atmospheric conditions. In the case of the parent HgBr_2 compound, it is well known that irradiation with ~ 200 nm UV light yields the monohalide (HgBr) with nearly 100% efficiency^{25,28–30}. Moreover, detailed quantum-chemical computations of the Cl- and Br-dihalides predict further efficient photodissociation at wavelengths²¹ longer than 200 nm. There are no comparable experimental or calculated photolysis data for the other HgBr-X compounds studied here. Nevertheless, a similar very efficient photodissociation step is to be expected for these mercury halides considering the even lower dissociation energies of the HgBr-X bond, as compared with that of the parent HgBr-Br dihalide (Supplementary Table 3)^{9,27}. In addition to this primary photolysis reaction to HgBr , it has been shown that $\text{Hg}(0)$ is also generated in the HgBr_2 photodissociation through direct or secondary channels, although to a much lesser extent^{31,32}. Based on this evidence, we consider in the atmospheric modelling below that HgBr is the main product of HgBrX photodissociation, although we also ran one scenario where HgBrX photodissociation results in $\text{Hg}(0)$ production.

Discussion

The absorption cross sections of *syn*- HgBrONO , HgBrOOH , HgBrOH , HgBr_2 , HgBrOCl , and HgBrOBr were implemented into the GEOS-Chem⁶ and GLEMOS^{33,34} global Hg chemistry and transport models (Methods), since these Hg(II) species are the most likely to be formed in the atmosphere^{6,11,27}. GEOS-Chem simulates Hg(II) as a single tracer, whereas GLEMOS simulates Hg(II) species individually. In GEOS-Chem the rapidly photolyzing Hg(II) species ($\text{HgBr-}[\text{ONO}, \text{OOH}, \text{OCl}, \text{OBr}]$) are calculated to be at pseudo-steady-state with HgBr . GLEMOS does

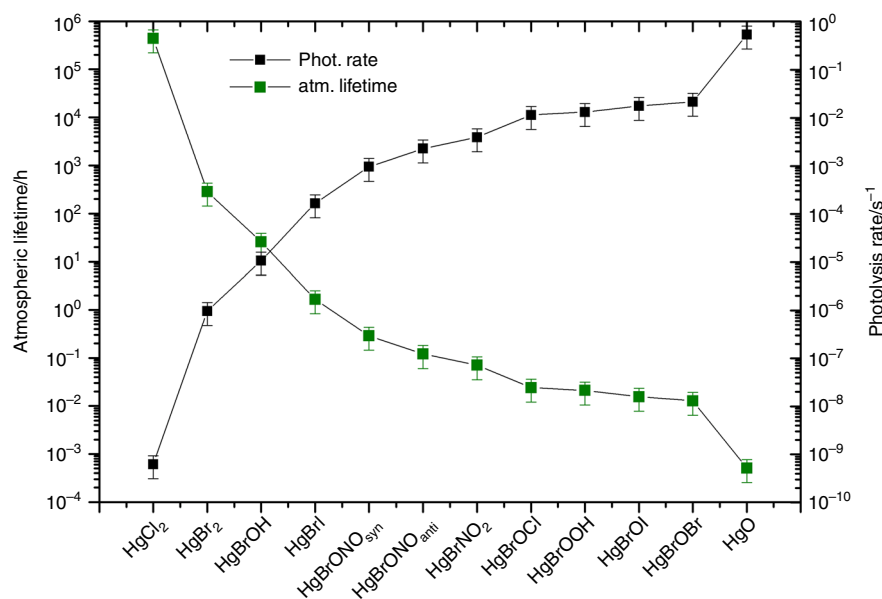


Fig. 4 Annually- and globally-averaged photolysis rate (s^{-1}) and lifetime (h) of Hg(II) compounds in the troposphere. Error bars correspond to one standard deviation

Table 1 Model test runs for different atmospheric Hg(II) reduction scenarios in the GLEMOS model

Run ID	Scenario
Run #1	No Hg(II) reduction
Run #2	Hg(II) reduction in aqueous phase using the experimentally derived rate constant (0.15 h^{-1}) in this study
Run #3	Gas phase Hg(II) photoreduction to Hg(0)
Run #4	Gas phase Hg(II) photoreduction to HgBr

not include the highly uncertain reduction reaction⁶ $\text{HgBr} + \text{NO}_2 \rightarrow \text{Hg(0)} + \text{BrNO}_2$. Omitting this reaction in GEOS-Chem lowers the Hg lifetime from 13 to 8 months in model Run#4 (The different model simulated scenarios for atmospheric Hg(II) reduction are shown in Table 1). *syn*-HgBrONO and HgBrOOH generally dominate the production of Hg(II) in both models (Supplementary Figure 3), whilst HgBr₂ becomes the prevalent Hg(II) species in the troposphere (Supplementary Figure 4) due to its longer lifetime against photolysis. Note that direct photoreduction to Hg(0) produces unrealistically long Hg lifetimes >19 months in both models. Therefore, photoreduction was considered to produce HgBr in all cases. Indeed, intensive photolysis of *syn*-HgBrONO and HgBrOOH causes HgBr to be a relevant species in the free troposphere (Supplementary Figure 5 and Fig. 5). HgBr can then be re-oxidized to gaseous Hg(II), or decay to Hg(0) by thermal dissociation, which is strongly dependent on pressure and temperature^{6,9}. Atmospheric aqueous Hg(II) reduction parameterizations in both models were capped with an upper limit that corresponds to our observed rainfall photoreduction rate constant, $k_{\text{red}} = 0.15 \text{ (h}^{-1}\text{)}$, leading to a 6% decrease in modelled atmospheric lifetime. Published model runs with capped aqueous phase Hg(II) reduction and without the gas-phase photoreduction^{6,33,34} yield total atmospheric Hg lifetimes of 4.9 and 4.6 months against deposition. Our new results show that gaseous Hg(II) photoreduction increases the Hg lifetime to 13 and 10 months in GEOS-Chem and GLEMOS model Run#4, respectively. We find that gas-phase photoreduction is the dominant reduction pathway.

We further examined the global atmospheric Hg(0) and Hg(II) distribution in GLEMOS. Figures 6 and 7 show the effect of the new photoreduction scheme on the global distribution of Hg(0) surface concentration. All these simulations were made with the previously assumed aqueous photoreduction mechanism removed. We find that simulations without the gaseous photoreduction lead to 35–40% underestimation of observed Hg(0) (Runs #1 and #2). The gas-phase Hg(II) photoreduction to Hg(0) (Run #3) results in unrealistically high Hg(0) concentrations with almost two-fold overestimation of the observations and strong underestimation of wet deposition. The model run with the incorporation of the gas phase photoreduction to HgBr (Run #4) shows that Hg(0) levels are 18% overestimated, and model Hg(II) wet deposition 20% underestimated with respect to observations (Fig. 7, Supplementary Table 4). The results of test Run#4 are closest to the observations which suggest that gas-phase reduction processes are important but also that re-oxidation via the HgBr intermediate is important. An additional step in the evaluation of model results can be made by examining the variability of modelled and observed Hg concentrations. Previous studies indicated that longer Hg(0) lifetimes lead to lower simulated Hg(0) variability, as represented by the standard deviation (1σ) of mean Hg(0) concentrations^{6,34}. Here, gas-phase photoreduction leads to simulated Hg(0) levels at the measurement sites ($1.62 \pm 0.36 \text{ ng/m}^3$, 1σ , STP) that have a larger standard deviation than observed Hg(0) ($1.38 \pm 0.25 \text{ ng/m}^3$, 1σ , STP). This indicates that the longer Hg(0) lifetime estimates of 8–13 months resulting from model Run#4 are broadly compatible with observed Hg(0) variability (1σ). The resulting global zonal distribution of Hg(0) and speciated Hg(II) (*syn*-HgBrONO, HgBrOOH, HgBrOH, HgBr, HgBr₂) reveals the major effects of gas-phase Hg(II) photoreduction in the global budget of atmospheric oxidized mercury (Supplementary Figures 4–9) and in the global patterns of mercury surface deposition (Fig. 8 and Supplementary Figure 10). In particular, it leads to a strong decrease of free tropospheric concentrations of *syn*-HgBrONO and HgBrOOH, which were previously considered as dominant Hg(II) species. In contrast, concentrations of HgBrOH and HgBr₂ increase due to the lower photolysis rates. The incorporation of gas-phase photoreduction leads to an increase in global Hg(0) deposition from

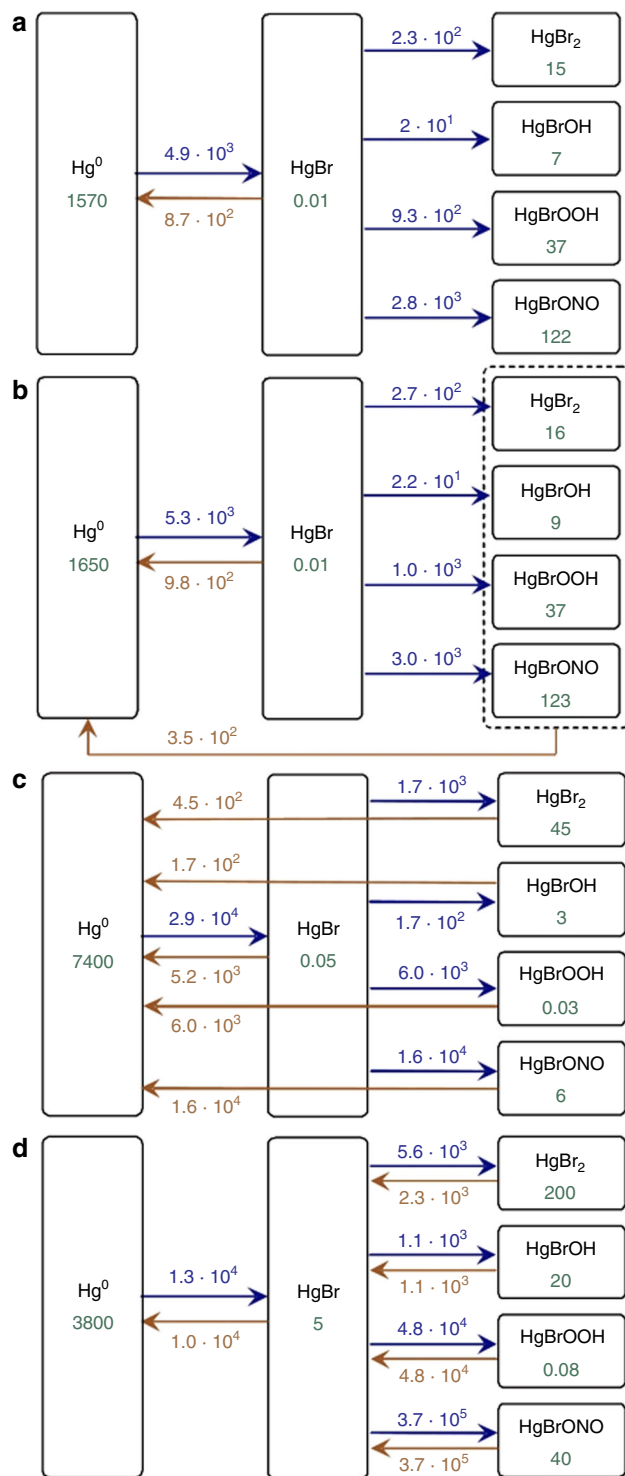


Fig. 5 Global budget of Hg chemical cycling covering the troposphere and lower stratosphere (up to ca. 30 kms) for different tests in GLEMOS: **a**—Run #1; **b**—Run #2; **c**—Run #3; **d**—Run #4. The mass estimates are in Mg, the fluxes are in Mg a⁻¹

11% (Run#1) to 24% (Run#4) at the expense of Hg(II) deposition (down by 13%, Fig. 8 and Supplementary Figure 10). We further observe a reduction of Hg deposition (dry and wet) to the ocean (down by 15%, Fig. 8 and Supplementary Figure 10), and an increase of Hg(0) dry deposition to the land surface (22%), particularly to vegetation in line with the recent findings that foliar uptake by vegetation drives continental Hg(0) seasonality⁷.

Global chemical budget diagrams (Fig. 5) summarize the Hg(0), Hg(I) and Hg(II) cycling in different model runs.

This work shows that the presence of an efficient gas-phase Hg (II) photoreduction challenges the current understanding of Hg cycling in the atmosphere and its deposition to the surface environment. We show that the new gas-phase Hg(II) photoreduction mechanism is likely the dominant reduction pathway for atmospheric mercury which can change the concept of the speciation of Hg(II) in the atmosphere. Its inclusion in state-of-the-art global models leads to significant modifications in the local scale deposition of Hg to the Earth's surface. As a result, enhanced deposition to land surfaces may prolong recovery of aquatic ecosystems long after Hg emissions are curbed, due to the longer residence time of Hg in soils than in oceans³⁵.

Methods

Computation of UV-Vis absorption spectra and cross sections. A theoretical methodology previously calibrated³⁶ was used for calculating the electronic absorption spectra and cross-sections of HgCl₂, HgBr₂, HgBrI, HgBrOBr, HgBrOI, HgBrOCl, HgBrNO₂, HgBrONO, HgBrOH, HgBrOOH, and HgO (The absorption cross sections are reported in Supplementary Data 2). Specifically, vertical transitions energies from the ground to electronically excited states and the corresponding oscillator strengths were computed with the highly accurate multireference complete-active-space self-consistent field/multistate complete-active-space second-order perturbation theory (CASSCF/MS-CASPT2) method³⁷, and the atomic-natural-orbital relativistic correlation-consistent valence triple- ζ plus polarization (the ANO-RCC-VTZP) basis set³⁸, taking into account scalar relativistic and spin-orbit coupling (SOC) effects (see below and Supplementary Table 5 for further details). Scalar relativistic effects were included by means of the third-order Douglas-Kroll and Hess (DKH3) Hamiltonian, and the spin-orbit coupling (SOC) was computed using the restricted active space state interaction (RASSI) method, as implemented in the MOLCAS 8 program³⁹.

The atmospheric modelling methods used in the present work require as input data the absorption cross sections of any compound that may undergo photolysis in the UV-VIS range under atmospheric conditions. To estimate the vibrational resolution and determine the band shapes, absorption spectra were generated for all the compounds studied here by sampling the nuclear coordinates of the ground-state equilibrium structure and frequencies according to a Wigner distribution, as described in refs 40,41 and subsequently computing the vertical transition energies and oscillator strengths at each structure. The Wigner distribution of geometries was obtained with the Newton-X 1.4 program^{42,43}, and an in-house program was used to compute the cross sections from the energies and oscillator strengths generated by the MOLCAS program. The ground-state structures and frequencies needed to generate the Wigner distribution were obtained by using the PBE0 functional⁴⁴ with the Def2TZVP basis set^{45–47} as implemented in the Gaussian 09 package⁴⁸. The minor differences observed in the simulated spectra due to ground-state geometries generated using either CASPT2, CCSD, or DFT methods are presented in Supplementary Figure 11.

For the di- and triatomic systems, appropriate symmetry point groups available in the MOLCAS program and which enabled for every possible displacement of atoms, were used in the calculations—C_{2v} in HgO and C_s in HgCl₂, HgBr₂, and HgBrI. For other studied systems, no symmetry was adopted (C₁ group). For each particular system, the number of spin-free states to account for in the CASSCF/MS-CASPT2 calculations were selected according to the energy criteria in such way to include all relevant electronic transitions up to 170 nm (and later apply SOC effects). All the parameters of the carried simulations of the spectra, such as the number of sampled geometries N_p, broadening of the Gaussian shape functions δ , and the numbers of included states per symmetry, are presented in detail in Supplementary Table 5.

By using the Wigner distribution of geometries for estimating the vibrational structure of the spectra and the CASSCF/MS-CASPT2/SO-RASSI methodology for determining the electronic structure, the agreement between computed and experimental transition energies was in the range of 5–10%, for those few cases in which gas-phase experimental data were available, namely for mercury compounds HgCl₂ and HgBr₂ (Fig. 3). The corresponding uncertainty in the calculated cross-section values is $\pm 25\%$ for the most intense transitions (see Fig. 3), similar to the actual dispersion of the experimental values^{22,24–26}.

The selected active spaces for the CASSCF/MS-CASPT2 computations are briefly discussed here. First general details are given and next we discuss those aspects which refer to each group of compounds.

According to our previous work on benchmarking the methodology for the representative HgBr₂ molecule³⁶ and on the basis of several test CASSCF computations with distinct active spaces for the whole set of molecules, some rules regarding the selection of the active spaces could be established.

First, for all the systems, s-subshell orbitals (and electrons) are not relevant in the studied energy range (up to 170 nm) and therefore were kept inactive and

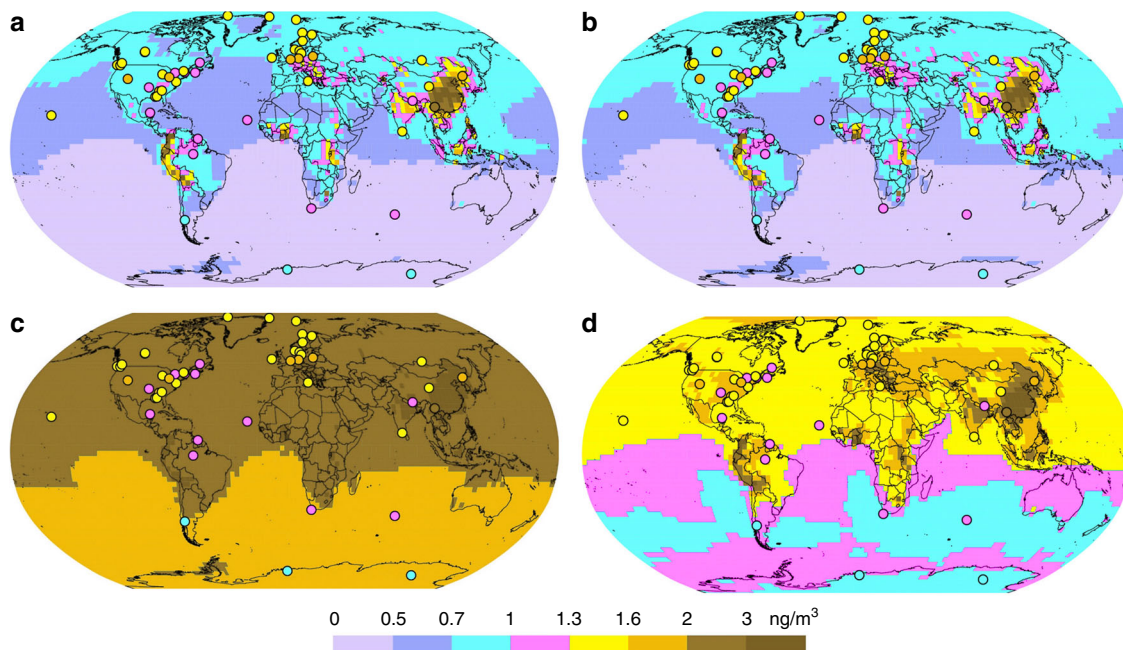


Fig. 6 Spatial distribution of Hg(O) surface concentration for different atmospheric Hg(II) reduction simulations in the GLEMOS model: **a** Run #1; **b** Run #2; **c** Run #3; **d** Run #4. Circles show observed values in the same colour scale. The measurement dataset is the same as in ref. ³⁵

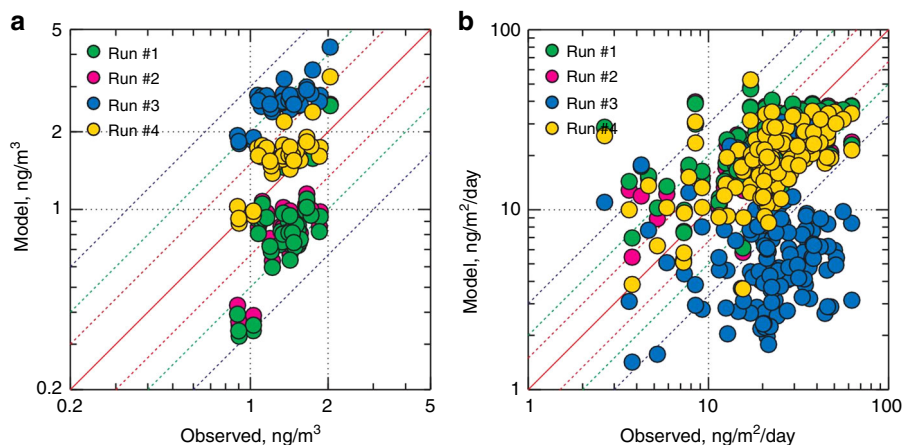


Fig. 7 Comparison between simulations from the GLEMOS model with measurements for the year 2013: **a** Hg(O) air concentration; **b** Hg(II) wet deposition. The measurement dataset is the same as in ref. ³⁵

doubly occupied, except for the 6s orbital of Hg, which has a key role in the transitions.

Second, the 5d orbitals of Hg are not involved in the transitions within the energy region of our interest, and therefore were not correlated in the CASSCF/MS-CASPT2 simulations for any system with the exception of the $1^1\Sigma$ and $1^3\Pi$ states of HgO. For this system, tests showed a small contribution of the 5d orbitals for high-energy transitions close to 170 nm.

Third, the two last natural orbitals (NOs) of non-bonding character, consisting on Br $4d_{xz/yz}$ + Br $4d_{xz/yz}$ atomic orbitals (AOs) and used in our first benchmark study on HgBr₂³⁶, were not necessary for the computations and were omitted in the di- and triatomic systems, in order to reduce computational effort.

Finally, the two last natural orbitals (NOs) of non-bonding character, consisting on Br $4d_{xz/yz}$ + Br $4d_{xz/yz}$ atomic orbitals (AOs) and used in our first benchmark study on HgBr₂³⁶, were not necessary for the computations and were omitted in the di- and triatomic systems, in order to reduce computational effort.

For each particular compound, the following criteria were adopted:

For HgCl₂, HgBr₂ and HgBrI, the optimal active spaces consisted of 12 electrons distributed in 10 NOs of the following character: σ/σ^* -type (Hg 6s ± Cl 3p_z/ Br 4p_z/ I 5p_z and Hg 6p_z ± Cl 3p_z/ Br 4p_z/ I 5p_z), σ^{nb} -type (Cl 3p_z/ Br 4p_z/ I 5p_z), and π^{nb} -type (Cl 3p_{x/y}/ Br 4p_{x/y}/ I 5p_{x/y} and Hg 6p_{x/y}). Although included in the active space, the σ^* orbital, Hg 6p_z ± Cl 3p_z/ Br 4p_z/ I 5p_z was not significantly occupied in the electronic configurations.

For $1^1\Sigma$ HgO and $3^1\Pi$ HgO the optimal active spaces consisted of 16 electrons distributed in 12 NOs. For these systems only, the active space additionally had to include 10 electrons belonging to the Hg 5d-subshell, and the remaining NOs were of the following type: σ/σ^* -type (Hg 6s ± O 2p_z and Hg 6p_z ± O 2p_z), and π^{nb} -type (O 2p_{x/y} and Hg 6p_{x/y}). In contrast to the other systems studied, σ^* Hg 6p_z + O 2p_z had an observable contribution in the configuration characterizing the excited states.

For HgBrOBr and HgBrOI the optimal active spaces consisted of 16 electrons distributed over 12 NOs. They correspond to the NOs formed by Hg 6s and AOs of p-type: O 2p_{x/y/z}, Br 4p_{x/y/z}/ I 5p_{x/y/z} and Hg 6p_{x/y}. Tests have shown that for the energy region of interest in the UV-VIS range, there are no relevant transitions to the Hg 6p_z orbital, and therefore it was not included in the active space to speed up the calculations.

For *syn*-HgBrONO and *anti*-HgBrONO and HgBrNO₂ isomers, the optimal active spaces consisted of 16 electrons distributed in 12 NOs. They correspond to NOs formed by Hg 6s and the AOs of p-type: O 2p_{x/y/z}, Br 4p_{x/y}/ I 5p_{x/y} and Hg 6p_{x/y}. Some orbitals from the valence space of the ONO and NO₂ groups had to be omitted due to the computational limitations. Tests have shown that for the relevant wavelength region in the UV-VIS, one σ -type bonding NO at the O-N-O and NO₂ groups of atoms remains doubly occupied and it was moved to the inactive space, whereas the Hg 6p_z orbital and higher σ^* -type virtual orbitals do not contribute significantly and therefore were kept in the secondary space.

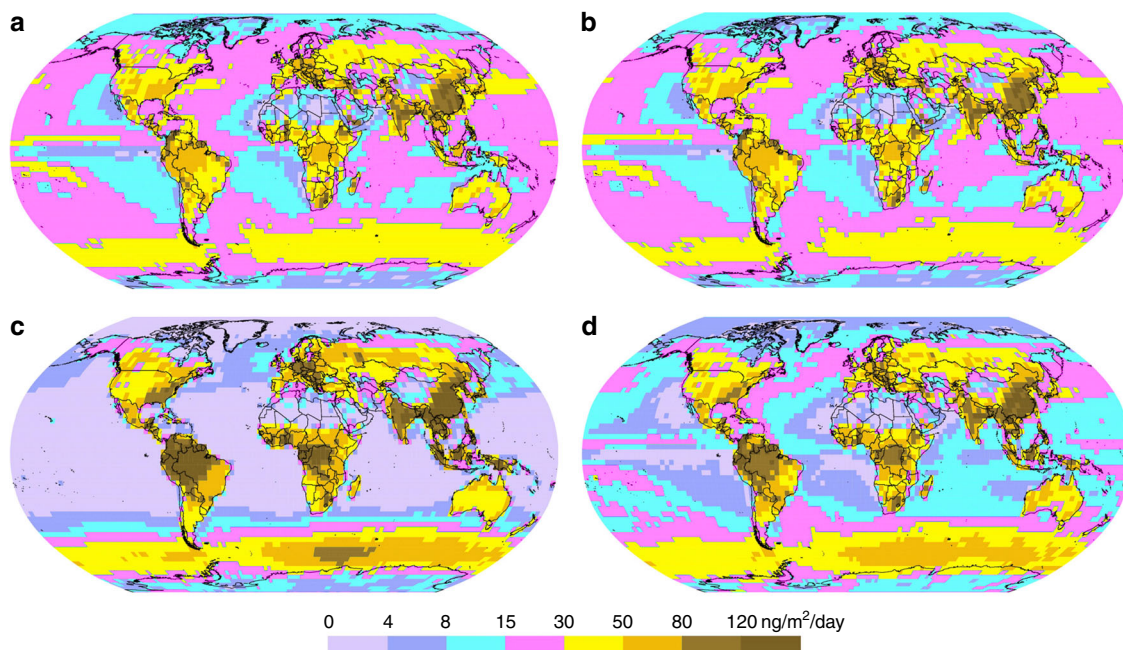


Fig. 8 Spatial distribution of total Hg (i.e. Hg(0) + Hg(II)) deposition for different tests in GLEMOS: **a**—Run #1; **b**—Run #2; **c**—Run #3; **d**—Run #4

In the case of HgBrOOH, the optimal active space was similar to those of HgBrOBr and HgBrOI. It consisted of 16 electrons distributed in 12 NOs formed by Hg 6s and AOs of p-type: O 2p_{x/y/z}, Br 4p_{x/y/z} and Hg 6p_{x/y/z}. As for in previous cases, the Hg 6p_z orbital was kept inactive since it was not relevant. In the case of HgBrOH, the appropriate active space was 12 electron distributed in 11 NOs.

To test the effect of the geometries used in the Wigner distribution on the simulated UV-VIS spectra, the optimization of the geometry of the ground state and the frequencies of normal modes were obtained using three different quantum-chemical methods for the representative HgBr₂ molecule:

- DFT/PBE0/Def2QZVP,
- CCSD/Def2QZVP, and
- SS-CASPT2(12,10)/ANO-RCC-VTZP.

Next, the computations of the electronic structure of the excited states were done for each set of geometries at the same level of theory: SOC-DKH3-MS-CASPT2(12,10)/ANO-RCC-VTZP. The same number of sampled geometries N_p and broadening of the Gaussian shape functions δ , were also chosen for the three sets of calculations: $N_p = 100$ and $\delta = 0.05$ eV, as shown in Supplementary Table 5.

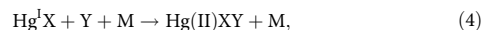
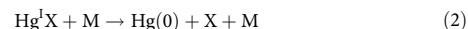
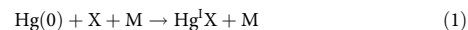
The UV-VIS absorption spectra obtained when using the differently generated sets of geometries is presented in Supplementary Figure 11 for HgBr₂. As can be seen, no significant differences are obtained, which validates the use of the less computationally costly method (DFT) for the simulations in the other molecules.

Computation of the photolysis rates. In this study we employ the global 3D chemistry-climate model CAM-Chem (Community Atmospheric Model with chemistry, version 4.0), to estimate the photolysis rate (J), and therefore the atmospheric lifetime ($\tau = 1/J$), of the different Hg(II) species according to their computed absorption cross section. The model includes a comprehensive chemistry scheme to simulate the evolution of trace gases and aerosols in the troposphere and the stratosphere⁴⁹. The model runs with the chlorine, iodine and bromine chemistry schemes from previous studies^{50–52}, including the photochemical breakdown of bromo- and iodo-carbons emitted from the oceans⁴⁹ and abiotic oceanic sources⁵³ of HOI and I₂. We have included all the Hg(II) species (HgCl₂, HgBr₂, HgBrI, HgBrOCl, HgBrOBr, HgBrOI, HgBrNO₂, HgBrONO (*syn* and *anti*), HgBrOH, HgBrOOH, and HgO) and their computed absorption cross sections. CAM-Chem has been configured in this work with a horizontal resolution of 1.9° latitude by 2.5° longitude and 26 vertical levels, from the surface to ~40 km altitude. The model run in this study was performed in the specified dynamics mode⁴⁹ using offline meteorological fields instead of an online calculation. This offline meteorology consists of a high-frequency meteorological input from a previous free running climatic simulation⁵⁴.

Description of the GEOS-Chem model. In this study, we use the GEOS-Chem Hg simulation from ref. ⁶ using the surface slab ocean boundary parametrization⁵⁵. The model calculates the transport and chemistry of tracer species Hg(0) and Hg(II). The parametrization of gas-particle partitioning of Hg(II) is from ref. ⁵⁶, and

the mercury redox chemistry (described in detail in Supplementary Table 6) includes Br- and Cl-initiated oxidation. Radical concentrations for Hg redox chemistry are from ref. ⁵⁷ with a diurnal cycle based on solar zenith angle imposed on top of monthly averages. Photolysis of HgBr-X species is calculated using the GEOS-Chem implementation⁵⁸ of the Fast-JX code⁵⁹.

Description of the GLEMOS model. For evaluation of the new Hg chemical mechanisms under the atmospheric conditions we apply the 3D multi-scale chemical transport model GLEMOS (Global EMEP Multi-media Modelling System). The model simulates atmospheric transport, chemical transformations and deposition of Hg species^{33,34,60}. In this study the model grid has a horizontal resolution 3° × 3° and covers troposphere and lower stratosphere up to 10 hPa (ca. 30 km) with 20 irregular terrain-following sigma layers. The atmospheric transport of the tracers is driven by meteorological fields generated by the Weather Research and Forecast modelling system (WRF)⁶¹ fed by the operational analysis data from the European Centre for Medium-Range Weather Forecasts (ECMWF) (ECMWF, 2018)⁶². In the current version the model transports Hg(0) and four Hg(II) species (HgBr₂, HgBrOH, HgBrOOH, HgBrNO₂) as separate species. Gas-particle partitioning of Hg(II) is parameterized following ref. ⁵⁶. A two-step mechanism of Hg(0) oxidation by Br in gas phase is included (ref. ⁶³):



The full reaction scheme is listed in Supplementary Table 6. Briefly, X ≡ Br is the first-step Hg(0) oxidant, Y is the second-step Hg(I) oxidant, and M is a molecule of air. The reaction rate constants are from: ref. ⁶⁴ for R1; ref. ⁹ for R2; ref. ⁶³ for Y ≡ Br in R3; ref. ¹² for Y ≡ Br and OH in R4; ref. ²⁷ for Y ≡ HO₂ and NO₂ in R4. Six-hourly concentration fields of Br are archived from a GEOS-Chem simulation⁶⁵, whereas OH, HO₂, NO₂, and particulate matter (PM_{2.5}) fields are imported from MOZART⁶⁶. The aqueous-phase chemistry includes oxidation^{10,67,68} of Hg(0) by dissolved O₃, OH and Cl(I)¹. We have included the gas-phase photoreduction of HgBr₂, HgBrOH, HgBrOOH, *syn*-HgBrONO using the rates calculated by CAM-Chem and the aqueous-phase photoreduction in cloud droplets with the photolysis rate constant 0.15 h⁻¹ estimated in this study. We perform simulations for the period 2007–2013 using anthropogenic emissions for 2010 (AMAP/UNEP, 2013)⁶⁹. Prescribed fluxes of Hg natural and secondary emissions from soil and seawater are generated depending on Hg concentration in soil, soil temperature and solar radiation for emissions from land and proportional

to the primary production of organic carbon in seawater for emissions from the ocean⁶⁰. The first 6 years of the period are used for the model spin up to achieve the steady-state Hg concentrations in the troposphere. The model results are presented as annual averages for 2013.

Description of rainfall Hg(II) gross reduction rate experiments. Ten rainfall events were sampled in suburban Toulouse and at the high mountaintop Pic du Midi Observatory (France) in the summer of 2017 using ultra-clean methods⁷⁰. Rainfall samples were transferred to a 0.5 L quartz reactor and illuminated with natural sunlight outdoors (up to 8 h), or with a solar simulator indoors (up to 48 h). Filtered samples were passed through a 0.45 micro-m quartz filter membrane to remove particles, in unfiltered samples this step was left out. Total Hg concentration of selected rainfall samples was augmented 10x with a NIST 3133 standard Hg solution, and equilibrated 24 h before light exposure. During light exposure, the quartz reactor was purged with Hg-free argon gas to remove product Hg(0). Reactant Hg(II) concentrations were measured in duplicate by cold vapour atomic fluorescence spectroscopy (CV-AFS) in 5 mL aliquots recovered from the reactor at fixed time steps and acidified to 0.04 M HCl, and 0.1 M BrCl. CV-AFS analysis accuracy was evaluated by regular analysis of the NRC ORMS-6 certified (25.6 ng L⁻¹) reference material with good results (24.8 ± 1.6 ng L⁻¹, 1σ, n = 33). Five out of twelve experiments showed increasing or constant reactant Hg(II) levels during the initial 2–4 hours, followed by a gradual decreasing in the final 24 h (Supplementary Data 1). These initial observations, tentatively explained by Hg(II)-DOM interaction with the quartz reactor wall, were not included in the rate constant calculation. This simplification did not affect the main outcome of this study. For further discussion on in-cloud Hg photoreduction see Supplementary Note.

Code availability. The code used in this study is available upon request.

Data availability

The data that supports the findings of this study is available upon request.

Received: 29 June 2018 Accepted: 11 October 2018

Published online: 15 November 2018

References

- Streets, D. G. et al. Total mercury released to the environment by human activities. *Environ. Sci. Technol.* **51**, 5969–5977 (2017).
- Pacyna, E. G. et al. Global emission of mercury to the atmosphere from anthropogenic sources in 2005 and projections to 2020. *Atmos. Environ.* **44**, 2487–2499 (2010).
- Deeds, D. A. et al. Development of a particle-trap preconcentration-soft ionization mass spectrometric technique for the quantification of mercury halides in air. *Anal. Chem.* **87**, 5109–5116 (2015).
- Ernest, C. T., Donohoue, D., Bauer, D., Schure, A. T. & Hynes, A. J. Programmable thermal dissociation of reactive gaseous mercury, a potential approach to chemical speciation: Results from a field study. *Atmosphere* **5**, 575–596 (2014).
- Ariya, P. A. et al. Mercury physicochemical and biogeochemical transformation in the atmosphere and at atmospheric interfaces: a review and future directions. *Chem. Rev.* **115**, 3760–3802 (2015).
- Horowitz, H. M. et al. A new mechanism for atmospheric mercury redox chemistry: Implications for the global mercury budget. *Atmos. Chem. Phys.* **17**, 6353–6371 (2017).
- Jiskra, M. et al. A vegetation control on seasonal variations in global atmospheric mercury concentrations. *Nat. Geosci.* **11**, 244–250 (2018).
- Global Mercury Assessment 2013: Sources, Emissions, Releases and Environmental Transport, UNEP: UNEP Chemicals Branch, Geneva, Switzerland, 2013.
- Dibble, T. S., Zelig, M. J. & Mao, H. Thermodynamics of reactions of ClHg and BrHg radicals with atmospherically abundant free radicals. *Atmos. Chem. Phys.* **12**, 10271–10279 (2012).
- Lin, C.-J. & Pehkonen, S. O. The chemistry of atmospheric mercury: a review. *Atmos. Environ.* **33**, 2067–2079 (1999).
- Wang, F. et al. Enhanced production of oxidised mercury over the tropical Pacific Ocean: a key missing oxidation pathway. *Atmos. Chem. Phys.* **14**, 1323–1335 (2014).
- Goodsite, M. E., Plane, J. & Skov, H. A theoretical study of the oxidation of Hg⁰ to HgBr₂ in the troposphere. *Environ. Sci. Technol.* **38**, 1772–1776 (2004).
- Holmes, C. D., Jacob, D. J. & Yang, X. Global lifetime of elemental mercury against oxidation by atomic bromine in the free troposphere. *Geophys. Res. Lett.* **33**, L20808 (2006).
- Shia, R. L., Seigneur, C., Pai, P., Ko, M. & Sze, N. D. Global simulation of atmospheric mercury concentrations and deposition fluxes. *J. Geophys. Res. Atmos.* **104**, 23747–23760 (1999).
- Qureshi A., MacLeod M., Sunderland E., Hungerbühler K. in *Environmental Chemistry and Toxicology of Mercury* (eds Liu, G. et al.) Ch. 12 (John Wiley & Sons, Inc., 2011).
- Pehkonen, S. O. & Lin, C.-J. Aqueous photochemistry of mercury with organic acids. *J. Air Waste Manag. Assoc.* **48**, 144–150 (1998).
- Seigneur, C., Vijayaraghavan, K. & Lohman, K. Atmospheric mercury chemistry: Sensitivity of global model simulations to chemical reactions. *J. Geophys. Res. Atmos.* **111**, D22306 (2006).
- Gärdfeldt, K. et al. Evasion of mercury from coastal and open waters of the Atlantic Ocean and the Mediterranean Sea. *Atmos. Environ.* **37**, 73–84 (2003).
- Lindqvist, O. et al. Mercury in the Swedish environment—recent research on causes, consequences and corrective methods. *Water Air Soil Pollut.* **55**, xi–261 (1991).
- Strömberg, D., Strömberg, A. & Wahlgren, U. Relativistic quantum calculations on some mercury sulfide molecules. *Water Air Soil Pollut.* **56**, 681–695 (1991).
- Wadt, W. R. The electronic structure of HgCl₂ and HgBr₂ and its relationship to photodissociation. *J. Chem. Phys.* **72**, 2469–2478 (1980).
- Maya, J. Ultraviolet absorption cross sections of HgI₂, HgBr₂, and tin (II) halide vapors. *J. Chem. Phys.* **67**, 4976–4980 (1977).
- Selin, N.E. Chemical cycling and deposition of atmospheric mercury: global constraints from observations. *J. Geophys. Res. Atmos.* **112**, D02308 (2007).
- Roxlo, C. & Mandl, A. Vacuum ultraviolet absorption cross sections for halogen containing molecules. *J. Appl. Phys.* **51**, 2969–2972 (1980).
- Schimitschek, E., Celto, J. & Trias, J. A. Mercuric bromide photodissociation laser. *Appl. Phys. Lett.* **31**, 608–610 (1977).
- Frantom, G., Bletzinger, P. & Garscadden, A. Measurement of the ultraviolet absorption cross-section of mercuric bromide. *Bull. Am. Phys. Soc.* **25**, 461 (1980).
- Jiao, Y. & Dibble, T. S. First kinetic study of the atmospherically important reactions BrHg' + NO₂ and BrHg' + HOO. *Phys. Chem. Chem. Phys.* **19**, 1826–1838 (2017).
- Erlanson, A. C. & Cool, T. A. On the regeneration mechanism of HgBr₂ in HgBr/HgBr₂ dissociation lasers. *Chem. Phys. Lett.* **96**, 685–689 (1983).
- Whitehurst, C. & King, T. Emission spectroscopy of mixed photodissociated mercury halides. *J. Phys. D. Appl. Phys.* **20**, 1577 (1987).
- Wilcomb, B., Burnham, R. & Djeu, N. UV absorption cross section and fluorescence efficiency of HgBr₂. *Chem. Phys. Lett.* **75**, 239–242 (1980).
- Baker, H. & Seddon, N. Transient absorption processes in a mercury bromide laser discharge. *J. Phys. D. Appl. Phys.* **21**, 1347 (1988).
- Schilowitz, A. M. & Wiesenfeld, J. R. Time-resolved study of mercury atom production and removal following the photolysis of HgBr₂ at 193 nm. *Chem. Phys. Lett.* **89**, 438–442 (1982).
- Travnikov, O. Contribution of the intercontinental atmospheric transport to mercury pollution in the Northern Hemisphere. *Atmos. Environ.* **39**, 7541–7548 (2005).
- Travnikov, O. et al. Multi-model study of mercury dispersion in the atmosphere: atmospheric processes and model evaluation. *Atmos. Chem. Phys.* **17**, 5271 (2017).
- Schuster, P. F. et al. Permafrost stores a globally significant amount of mercury. *Geophys. Res. Lett.* **45**, 1463–1471 (2018).
- Sitkiewicz, S. P. et al. Ab initio quantum-chemical computations of the electronic states in HgBr₂ and IBr: Molecules of interest on the Earth's atmosphere. *J. Chem. Phys.* **145**, 244304 (2016).
- Finley, J., Malmqvist, P.-Å., Roos, B. O. & Serrano-Andrés, L. The multi-state CASPT2 method. *Chem. Phys. Lett.* **288**, 299–306 (1998).
- Roos, B. O., Lindh, R., Malmqvist, P.-Å., Veryazov, V. & Widmark, P.-O. Main group atoms and dimers studied with a new relativistic ANO basis set. *J. Phys. Chem. A* **108**, 2851–2858 (2004).
- Aquilante, F. et al. Molcas 8: New capabilities for multiconfigurational quantum chemical calculations across the periodic table. *J. Comput. Chem.* **37**, 506–541 (2016).
- Barbatti, M., Aquino, A. J. & Lischka, H. The UV absorption of nucleobases: semi-classical ab initio spectra simulations. *Phys. Chem. Chem. Phys.* **12**, 4959–4967 (2010).
- Crespo-Otero, R. & Barbatti, M. Spectrum simulation and decomposition with nuclear ensemble: formal derivation and application to benzene, furan and 2-phenylfuran. *Theor. Chem. Acc.* **131**, 1237 (2012).
- Barbatti, M. et al. The on-the-fly surface-hopping program system Newton-X: Application to ab initio simulation of the nonadiabatic photodynamics of benchmark systems. *J. Photochem. Photobiol. A: Chem.* **190**, 228–240 (2007).
- Barbatti, M. et al. Newton-X: a surface-hopping program for nonadiabatic molecular dynamics. *Wiley Interdiscip. Rev.: Comput. Mol. Sci.* **4**, 26–33 (2014).

44. Adamo, C. & Barone, V. Toward reliable density functional methods without adjustable parameters: The PBE0 model. *J. Chem. Phys.* **110**, 6158–6170 (1999).
45. Andrae, D., Haeussermann, U., Dolg, M., Stoll, H. & Preuss, H. Energy-adjusted ab initio pseudopotentials for the second and third row transition elements. *Theor. Chem. Acc.: Theory, Comput., Model. (Theor. Chim. Acta)* **77**, 123–141 (1990).
46. Peterson, K. A., Figgen, D., Goll, E., Stoll, H. & Dolg, M. Systematically convergent basis sets with relativistic pseudopotentials. II. Small-core pseudopotentials and correlation consistent basis sets for the post-d group 16–18 elements. *J. Chem. Phys.* **119**, 11113–11123 (2003).
47. Weigend, F. & Ahlrichs, R. Balanced basis sets of split valence, triple zeta valence and quadruple zeta valence quality for H to Rn: Design and assessment of accuracy. *Phys. Chem. Chem. Phys.* **7**, 3297–3305 (2005).
48. Frisch, M. et al., *Gaussian 09, revision D. 01*. (Gaussian, Inc., Wallingford CT, 2009).
49. Ordóñez, C. et al. Bromine and iodine chemistry in a global chemistry–climate model: description and evaluation of very short-lived oceanic sources. *Atmos. Chem. Phys.* **12**, 1423–1447 (2012).
50. Fernandez, R. P., Salawitch, R. J., Kinnison, D. E., Lamarque, J. F. & Saiz-Lopez, A. Bromine partitioning in the tropical tropopause layer: implications for stratospheric injection. *Atmos. Chem. Phys.* **14**, 13391–13410 (2014).
51. Saiz-Lopez, A. et al. Iodine chemistry in the troposphere and its effect on ozone. *Atmos. Chem. Phys.* **14**, 13119–13143 (2014).
52. Saiz-Lopez, A. et al. Injection of iodine to the stratosphere. *Geophys. Res. Lett.* **42**, 6852–6859 (2015).
53. Prados-Roman, C., Cuevas, C. A., Fernandez, R. P., Kinnison, D. E., Lamarque, J. F. & Saiz-Lopez, A. A negative feedback between anthropogenic ozone pollution and enhanced ocean emissions of iodine. *Atmos. Chem. Phys.* **15**, 2215–2224 (2015).
54. Gent, P. R. et al. The community climate system model version 4. *J. Clim.* **24**, 4973–4991 (2011).
55. Soerensen, A. L. et al. An improved global model for air–sea exchange of mercury: High concentrations over the North Atlantic. *Environ. Sci. Technol.* **44**, 8574–8580 (2010).
56. Amos, H. M. et al. Gas–particle partitioning of atmospheric Hg (II) and its effect on global mercury deposition. *Atmos. Chem. Phys.* **12**, 591–603 (2012).
57. Schmidt, J. A. et al. Modeling the observed tropospheric BrO background: Importance of multiphase chemistry and implications for ozone, OH, and mercury. *J. Geophys. Res. Atmos.* **121**, 11819–11835 (2016).
58. Eastham, S. D., Weisenstein, D. K. & Barrett, S. R. Development and evaluation of the unified tropospheric–stratospheric chemistry extension (UCX) for the global chemistry–transport model GEOS-Chem. *Atmos. Environ.* **89**, 52–63 (2014).
59. Bian, H. & Prather, M. J. Fast-J2: Accurate simulation of stratospheric photolysis in global chemical models. *J. Atmos. Chem.* **41**, 281–296 (2002).
60. Travníkov O. & Ilyin I. The EMEP/MSC-E mercury modeling system. In *Mercury Fate and Transport in the Global Atmosphere* (eds Mason R. & Pirrone N.) 571–587 (Springer, Boston, 2009).
61. Skamarock W. C. et al. A description of the advanced research WRF version 2. NCAR Technical Note, NCAR/TN-468+STR. (National Center For Atmospheric Research, Mesoscale and Microscale Meteorology Div, Boulder, Co, 2005).
62. ECMWF: European Centre for Medium-Range Weather Forecasts (datasets available from <http://www.ecmwf.int/en/forecasts/datasetA>).
63. Balabanov, N. B., Shepler, B. C. & Peterson, K. A. Accurate global potential energy surface and reaction dynamics for the ground state of HgBr₂. *J. Phys. Chem. A* **109**, 8765–8773 (2005).
64. Donohoue, D. L., Bauer, D., Cossairt, B. & Hynes, A. J. Temperature and pressure dependent rate coefficients for the reaction of Hg with Br and the reaction of Br with Br: A pulsed laser photolysis-pulsed laser induced fluorescence study. *J. Phys. Chem. A* **110**, 6623–6632 (2006).
65. Parrella, J. et al. Tropospheric bromine chemistry: implications for present and pre-industrial ozone and mercury. *Atmos. Chem. Phys.* **12**, 6723–6740 (2012).
66. Emmons L. K. et al. Description and evaluation of the Model for Ozone and Related Chemical Tracers, version 4 (MOZART-4). (2010).
67. Gärdfeldt, K., Sommar, J., Strömberg, D. & Feng, X. Oxidation of atomic mercury by hydroxyl radicals and photoinduced decomposition of methylmercury in the aqueous phase. *Atmos. Environ.* **35**, 3039–3047 (2001).
68. Munthe, J. The aqueous oxidation of elemental mercury by ozone. *Atmos. Environ. Part A General. Top.* **26**, 1461–1468 (1992).
69. AMAP/UNEP. Technical Background Report for the Global Mercury Assessment 2013. *Arctic Monitoring and Assessment Programme*, Oslo, Norway/UNEP Chemicals Branch, Geneva, Switzerland. vi+263pp (2013).
70. Enrico, M. et al. Atmospheric mercury transfer to peat bogs dominated by gaseous elemental mercury dry deposition. *Environ. Sci. Technol.* **50**, 2405–2412 (2016).

Acknowledgements

This work was supported by the Consejo Superior de Investigaciones Científicas (CSIC) Spain. The National Center for Atmospheric Research (NCAR) is funded by the National Science Foundation (NSF). Computing resources were provided by the Climate Simulation Laboratory at NCAR's Computational and Information Systems Laboratory (CISL), sponsored by the NSF, provided computing resources. The CESM project (which includes CAM-Chem) is supported by the NSF and the office of Science (BER) of the US Department of Energy. This study has received funding from the European Research Council Executive Agency under the European Union's Horizon 2020 Research and innovation programme (Projects 'ERC-2016-COG 726349 CLIMAHAL' to A.S.L. and 'ERC-2010-STG 258537' to J.E.S.), and from H2020 ERA-PLANET 689443. S.P.S. acknowledges the Basque Government for funding through a PhD fellowship (PRE 2017 1 0403). D.R.S. is thankful to the Spanish Ministerio de Economía y Competitividad (MINECO) (Projects CTQ2017-87054-C2-2-P, RYC-2015-19234 grant, and Unit of Excellence María de Maeztu MDM-2015-0538). J.M.O.-E. is grateful to program "Salvador de Madariaga" Project No. PRX17/00488 (Ministerio de Educación, Cultura y Deporte). We thank the UMS 831 Pic du Midi Observatory team for help with rainwater sampling and Franck Gilbert for use of the solar simulator.

Author contributions

A.S.-L. and J.E.S. conceived the experiments. S.P.S. and D.R.S. performed the quantum-chemical simulations. C.A.C. and D.E.K. performed the global photolysis rate calculations. M.J. and Y.X. conducted the aqueous photoreduction experiments. C.P.T., E.M.S., D.J.J., and O.T. performed the mercury chemical transport model simulations. A.S.-L., S.P.S., D.R.S., J.M.O., J.Z.D., R.N., J.M.C.P., C.A.C., D.E.K., F.W., D.R., A.U.A., J.E.S., C.P.T., E.M.S., D.J.J., and O.T. analysed and interpreted both the quantum-chemical and atmospheric results. All authors contributed to paper writing.


Additional information

Supplementary Information accompanies this paper at <https://doi.org/10.1038/s41467-018-07075-3>.

Competing interests: The authors declare no competing interests.

Reprints and permission information is available online at <http://npg.nature.com/reprintsandpermissions/>

Publisher's note: Springer Nature remains neutral with regard to jurisdictional claims in published maps and institutional affiliations.

 **Open Access** This article is licensed under a Creative Commons Attribution 4.0 International License, which permits use, sharing, adaptation, distribution and reproduction in any medium or format, as long as you give appropriate credit to the original author(s) and the source, provide a link to the Creative Commons license, and indicate if changes were made. The images or other third party material in this article are included in the article's Creative Commons license, unless indicated otherwise in a credit line to the material. If material is not included in the article's Creative Commons license and your intended use is not permitted by statutory regulation or exceeds the permitted use, you will need to obtain permission directly from the copyright holder. To view a copy of this license, visit <http://creativecommons.org/licenses/by/4.0/>.

© The Author(s) 2018